JOURNAL OF AIRCRAFT
Vol. 47, No. 5, September–October 2010

Crack-Tip Behavior in Fiber/Metal Laminates by Means of Digital-Image Correlation

R. Rodi*
Materials Innovation Institute, 2628 CD Delft, The Netherlands
and
R. C. Alderliesten† and R. Benedictus‡
Delft University of Technology, 2629 HS Delft, The Netherlands

DOI: 10.2514/1.C000223

This paper presents the study on the crack-tip behavior in fiber/metal laminates under static loading. The effect on the strain field due to the variation of layup and fiber/preimpregnated has been analyzed. The strain field has been measured using digital-image correlation and evaluated by comparing it with the strain field predicted with finite-element analysis, which provided information about the interlaminar shear mechanisms. In addition, the paper demonstrates the power of the digital-image correlation technique for in situ strain measurements, offering new insight into the damage mechanisms that prevail in fiber/metal laminates under static loading.

Nomenclature

E_{lam}	=	laminate stiffness
E_{11}	=	tensile modulus in longitudinal direction
E_{22}	=	tensile modulus in transversal direction
FVF_{f0°	=	fiber volume fraction at 0°
G_{12}	=	shear modulus
α	=	coefficient of thermal expansion
$\varepsilon_{\text{break}}$	=	strain at failure
$\varepsilon_{0.2}$	=	strain at yield
$\nu_{1.2}$	=	Poisson's ratio
$\sigma_{f0^\circ}^{\text{cur}}$	=	residual stress in the 0° fiber layer due to curing
σ_m^{cur}	=	residual stress in the metal layer due to curing
σ_{ult}	=	ultimate stress
$\sigma_{0.2}$	=	yield stress

I. Introduction

UNDERSTANDING of the behavior of structural materials under static load is important when assessing the damage tolerance of the structural design of an aircraft. An important example of structural material characterization under static loading is the residual strength evaluation, which is required by the airworthiness regulations [1] to show that the remaining structure is able to withstand the operational loads, even in presence of severe damage. The analysis of residual strength in the presence of large fatigue cracks or accidental damage is thus of primary importance for an aircraft structural design. A lot of research [2–5] has been carried out in the past to investigate the residual strength of fiber/metal laminates (FMLs). It has been pointed out that the composite nature of FMLs (metal/fiber combination) increases the complexity of the problem, because more constituents act together to redistribute the applied load, especially when large-scale yielding develops in the metal layers. The extensive investigations carried out by Vermeeren [2] and de Vries [3] and de Vries and Vlot [4] have provided detailed qualitative descriptions of the failure mechanisms inside FMLs under static load.

Although de Vries [3] also proposed a semiempirical approach to predict the residual strength in FMLs, the natural step toward the development of a generic analytical prediction model for residual strength requires a full understanding and quantification of the main failure mechanisms occurring during the quasi-static-load sequence, like the delamination at the fiber/metal interface, plastic zone, metal cracking, and fiber failure.

This paper presents the experimental investigation and finite-element (FE) analysis of the crack-tip behavior in different types of FMLs under static loading. The influence of different layups and fibers/preimpregnated (prepreg) systems on the FML behavior has been analyzed. A digital-image correlation (DIC) tool [6], recently developed at Delft University of Technology, was employed in order to measure the complete crack-tip strain field of the FML, including the plastic zone shape and its extension, due to increments of static load. The stepwise load increments were limited during the tests until crack initiation. FE analysis (FEA) was performed by simulating the experimental tests. No crack extension or failure mechanisms were implemented into the FE model. Besides the validation of the FE model, the FEA provided qualitative information with regard to the load transfer mechanisms at the fiber/metal interface. Such information is not provided by the DIC results, since they refer only to the deformation on the external metal layer.

The present investigation and the validation of the FE model provide a basis for the development of an analytical prediction model for residual strength in FMLs.

II. Crack-Tip Behavior in Fiber/Metal Laminates Under Static-Load Condition

FMLs are hybrid materials consisting of thin metal layers with fiber/epoxy layers in between, which have been developed in the past to increase the fatigue resistance of laminated aluminum structures by adding fibers in the bond line [5,7,8] (see Fig. 1).

The failure process in FMLs under static loading involves complex phenomena that increase the difficulty of the analysis. Vermeeren [2], de Vries [3], and de Vries and Vlot [4] provided a detailed description of the quasi-static failure sequence in glare. They subdivided the failure sequence into four principal mechanisms:

1) Crack initiation in the metal layer accompanied by a large amount of plastic deformation (crack-tip blunting). The large amount of plastic deformation might be accompanied by static delamination at the fiber/metal interface.

Presented as Paper 2009-2586 at the 50th AIAA/ASME/ASCE/AHS/ASC Structures, Structural Dynamics, and Materials Conference, Palm Springs, CA, 4–7 May 2009; received 9 December 2009; accepted for publication 8 March 2010. Copyright © 2010 by the American Institute of Aeronautics and Astronautics, Inc. All rights reserved. Copies of this paper may be made for personal or internal use, on condition that the copier pay the $10.00 per-copy fee to the Copyright Clearance Center, Inc., 222 Rosewood Drive, Danvers, MA 01923; include the code 0021-8669/10 and $10.00 in correspondence with the CCC.

*Ph.D. Researcher; r.rodi@m2i.nl.
†Assistant Professor, Structural Integrity, Faculty of Aerospace Engineering; R.C.Alderliesten@tudelft.nl.
‡Professor, Structural Integrity, Faculty of Aerospace Engineering; R.Benedictus@tudelft.nl.

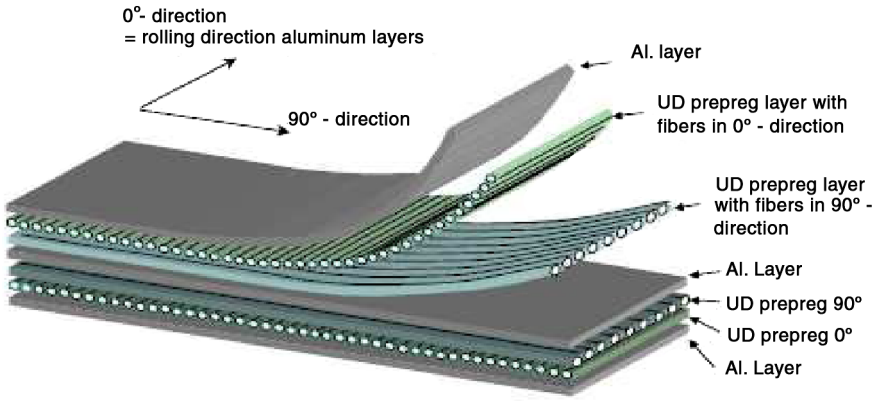

Fig. 1 Typical layup for a cross-ply FML [2].

2) Stable crack extension in the metal layers characterized by the absence of crack-tip blunting.

3) Local fiber failure characterized by the strain to failure of the fiber/prepreg system.

4) Final failure accompanied by dynamic delamination.

All these mechanisms are strongly influenced by the strain field in front of the crack tip. For high static loads, the plastic component of the strain field plays a fundamental role, because stress redistribution mechanisms will take place in the vicinity of the yielded metal. In this condition, the yielded metal loses the capability to carry the load, and part of the load is transferred from the yielded metal to both the elastic fiber layers and the remaining elastic part of the metal layers. This load-redistribution mechanism ensures higher performance of FMLs with respect to an equivalent monolithic metal panel when high static loads are applied.

III. Description of Experiments

In the following sections, the experiments are described with respect to materials, test procedure, and applied measurement technique. Here, special attention will be given to the DIC technique that has been used. Details on the analysis of images are provided.

A. Test Matrix and Materials

Several tests have been performed on a central crack tension specimen made by different kinds of FMLs. In Table 1, the mechanical properties of the selected materials are presented.

As shown in Table 1, the property range of the selected materials was chosen such that a significant variation of the fiber parameters, like stiffness, elongation at break, and coefficient of thermal expansion (CTE), was obtained. The use of two different epoxy resin systems (DT120 and FM94) was due to the direct availability at that moment of those materials.

Tensile tests on a 2024-T3 laminated specimen were performed to obtain the stress/strain curve used as input for the FEA. To obtain values that better describe the behavior of the thin metal layers present in the FML, the tensile test specimens were manufactured by bonding together four 0.4-mm-thick metal layers by using the FM94 epoxy adhesive film. The tensile tests were performed according to the American Society for Testing and Materials standard procedure [9] but, in this case, the actual stress was calculated based on the total metal thickness only, excluding the adhesive thickness, since the contribution of the adhesive layer is negligible. Figure 2 illustrates the strain–stress curve for such a laminate together with the power law trend curve that was used as the input parameter for the FEA.

Table 1 Material parameters (UD denotes unidirectional)

Properties	UD M30SC/ DT120[a]	UD Zylon/ FM94[b]	UD S2 Glass/ FM94[b]	AA2024-T3
E_{11}, GPa	155	120	50.6	72.4
E_{22}, GPa	7.8	2.84	9.4	——
G_{12}, GPa	5.5	1.04	5.55	27.6
$\sigma_{0.2}$, MPa	——	——	——	345
σ_{ult}, MPa	1800	2261	2640	480
ν_{12}	0.27	0.22	0.33	0.33
ε_{break}, %	1.6	2	4.5	15–18
$\varepsilon_{0.2}$, %	——	——	——	0.55
α	$-0.45 \cdot 10^{-6}$	$-6 \cdot 10^{-6}$	$5.6 \cdot 10^{-6}$	$25 \cdot 10^{-6}$
ρ, g/cm^3	1.76	1.54	1.98	2.78

[a]Data available online at http://www.delta-tech.it [retrieved 2008].
[b]Data available online at http://www.cytec.com [retrieved 2008].

The analysis of the crack-tip behavior was performed on five panels manufactured by bonding together the selected materials, as summarized in Table 2. The geometry of each panel is illustrated in Fig. 3.

The specimen geometry was the same for all the configurations and, in order to avoid even small differences, the saw cut was made by milling. Because of the high strain gradient that develops in front of the crack tip, even a small difference in the saw-cut length could have strongly influenced the strain values in front of the crack tip. In this fashion, as it will be explained in the next sections, the comparison between the FEA and the DIC results is not affected by geometrical differences.

The bonding process was carried out in an autoclave, at a temperature of 120°C, at a maximum pressure of 6 bar. The difference in CTE between metal and fiber/prepreg causes residual stresses in the laminate after curing. At 120°C, the epoxy resin starts to solidify by building cross links in the material. When cooling down from the initial (assumed) stress-free temperature at 120°C, the constituent with the highest CTE (metallic constituent) shrinks more than the other one (composite constituent). The contraction is prevented, leading a state of tension in the metallic constituent and compression in the composite constituent [5,8,10]. The calculation of the residual stresses was carried out by means of classical laminate theory (CLT), as described in [10], and the results are presented in Table 2.

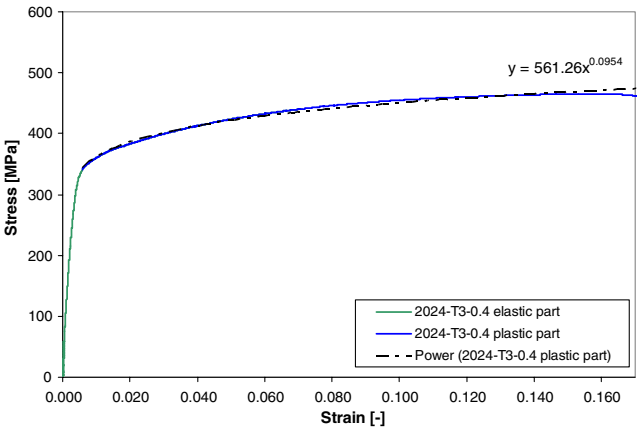

Fig. 2 Stress/strain curve for laminated 2024-T3 (thickness of each layer $t = 0.4$ mm).

Table 2 Test matrix and material characteristics (MVF denotes metal volume fraction)

Spec.	Layup	Materials	t_{tot}, mm	t_{pp}, mm	Characteristics[a] MVF	$FVF_{f0°}$	E_{lam}, GPa	σ_m^{cur}, MPa	$\sigma_{f0°}^{cur}$, MPa
1	FML 3-3/2-.4	2024-T3/FM94/S2 glass	1.75	0.137	0.69	0.15	65.3	15	−78
2	FML 3-3/2-.4	2024-T3/FM94/Zylon	1.82	0.156	0.65	0.175	75.2	52	−235
3	FML 3-3/2-.4	2024-T3/DT120/M30SC	1.82	0.156	0.65	0.175	83.2	59	−236
4	FML 2-3/2-.4	2024-T3/FM94/S2 glass	1.75	0.137	0.69	0.31	72.8	30	−89
5	ML 3-3/2-.4	2024-T3/FM94	1.65	0.11	1	——	——	——	——

[a]The calculation of the characteristics listed in the table is based on the CLT [10].

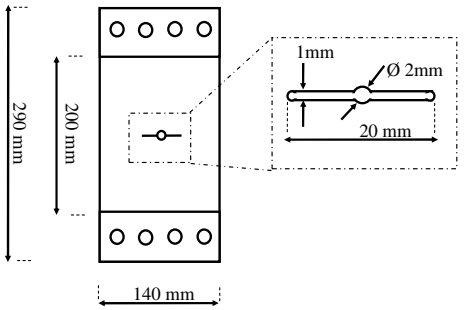

Fig. 3 Geometry of the test specimens.

B. Test Setup and Measurement Technique

A digital camera system with an *x-y-z* electronically controlled table was used to perform the digital-image acquisition of the area in front of the crack tip (see Fig. 4).

The images were captured at different static loads and stored. Figure 4 illustrates the procedure followed during the test execution. To reach fixed load/stress levels, the load increment step was performed under force control, while the images where captured under displacement control. This procedure enabled to keep the control of the crack-tip deformation, especially when high loads were applied, to avoid undesired crack propagation.

C. Digital-Image Correlation Method

DIC is a technique to obtain the deformation fields on an object surface [6,11,12]. DIC has advantages with respect to the standard

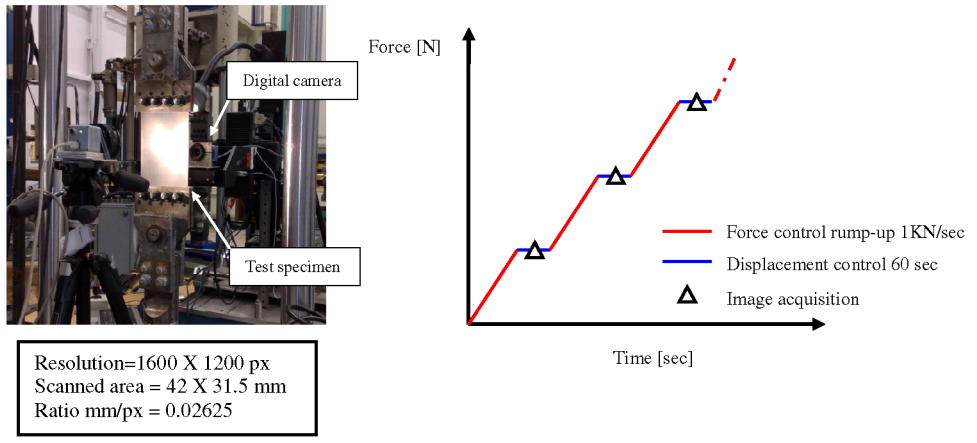

Fig. 4 Test setup and test execution.

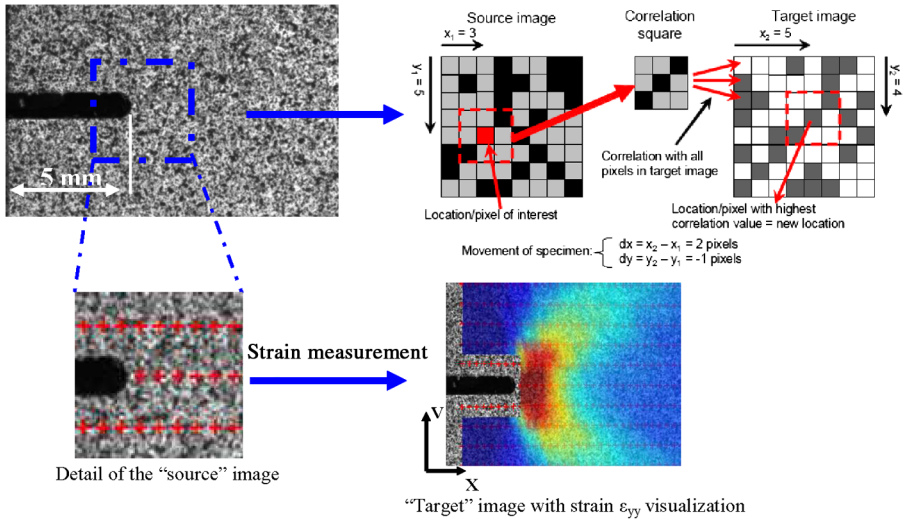

Fig. 5 Schematic overview of the correlation process for one pixel and strain measurement [6].

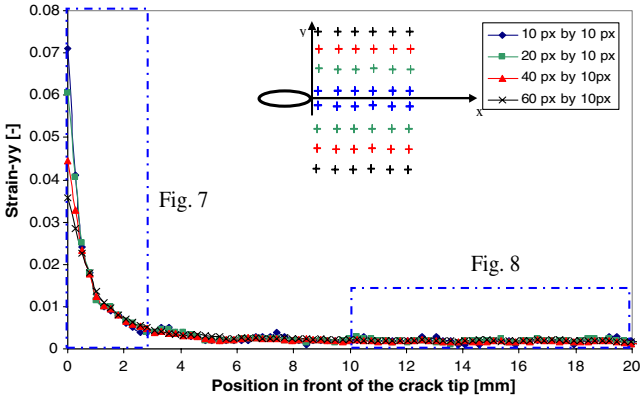

Fig. 6 Influence on the strain gradient $\varepsilon_{yy}(x)$ due to the distance between the grid points.

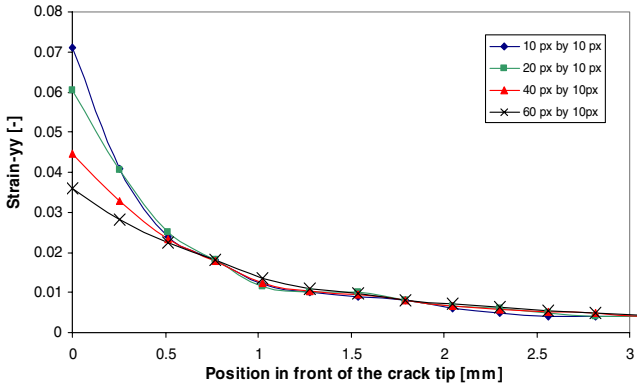

Fig. 7 Crack-tip strain values influenced by the distance between grid points.

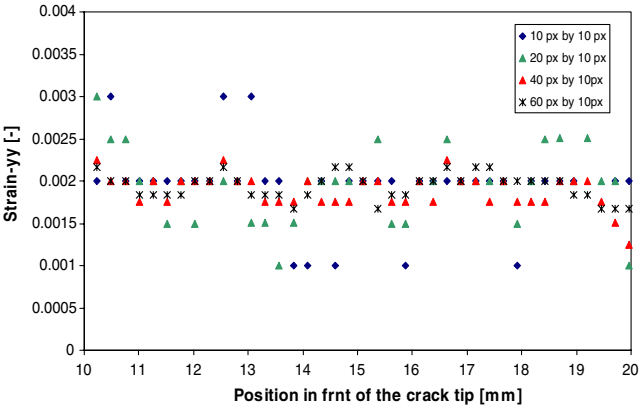

Fig. 8 Scatter dependency on the distance between grid points.

strain measurements systems, like strain gauges, extensometers, etc., simply because it is the one of the few strain measurement methods that can provide local quantitative strain data of large surface areas. The DIC tool [6] used for the image correlation uses digital grid points that mark specific positions (pixels) on the specimen surface when no deformation is present (source image). Those positions are traced back during the test defining the current displacement field in each image (target image). Figure 5 schematically illustrates the correlation procedure. The postprocessing of the obtained displacement fields provides the relative strain field.

To obtain an effective correlation, a speckled pattern was applied by using black and white paint, as shown in Fig. 5. The importance of using a speckled pattern is twofold. First, it ensures a higher correlation, thus improving the accuracy of the measurement. Second, it prevents changes in the surface light reflection when high deformation paths develop. As described in [6], the error in the DIC tool is in the order of 0.02 to 0.1 px, depending on the quality of the image and the surface of the specimen. The influence of this error on the strain can be affected by changing the distance between the grid points and, thus, the gauge length. The error of the DIC can induce scatter in the data when the magnitude of the measured strain value is similar to the error itself.

Because the strain gradient ahead of the crack tip reaches very high values, a sensitivity analysis was performed in order to study the effect of the grid-point distance on the strain results. Two considerations are made. First, the measured strain values ε_{yy} at the crack tip are affected by the distance in y direction between each couple of grid points. Because of the high strain gradient in the y direction, a realistic strain measurement requires a relatively small distance in the y direction between the grid points. Second, a reduction of the distance between each couple of grid points introduces a greater error in the strain measurements. If the error is of the same order of magnitude of the measured strain, it is possible to obtain significant scatter in the data.

Figure 6 shows the results of the sensitivity analysis performed on the laminated aluminum specimen by varying the distance in the y direction between each couple of grid points placed along the line in front of the crack tip. The distance in the y direction was changed from 10 to 60 px, while the distance in the x direction was fixed at 10 px. From Fig. 7, it is clear that a reduction of the distance in the y direction increases the local strain value in front of the crack tip. On the other hand, a small distance between the grid points increases the scatter in the results as the actual strain value gets close to the error (see Fig. 8). Table 3 provides a simple comparison of the results extrapolated from Fig. 6.

The sensitivity analysis provided information on how to optimize the distribution of the grid points along the scanned area to improve the measurement results and to reduce the computing time needed for the correlation. As result, in front of the crack tip, a distance in the y direction varying between 10 to 40 px was used, while a fixed distance of 70 px was used in the rest of the scanned area (see Fig. 9). The distance in the x direction was fixed at 20 px.

To prove the validity of the DIC measurements, a comparison with the data obtained with strain gauges was made. As illustrated in Fig. 10, four strain gauges were bonded in front of the crack tip on one side of the panel at a distance of 15 mm from each other. DIC measurements were performed on the other side of the panel, following the procedure previously explained. Figure 10 illustrates a very good agreement between DIC and strain gauge results for two different stress levels. The DIC technique is even more accurate than the strain gauges in those areas where high strain gradients are

Table 3 Sensitivity analysis results

		$\varepsilon_{\text{crack tip}}$		Scatter bandwidth	
No.	Config.	Value	Diff. %	Value	Diff. %
1	10 × 10 px	0.071	——	0.002	——
2	20 × 10 px	0.060	−15%	0.001	−50%
3	40 × 10 px	0.044	−37%	0.0004	−80%
4	60 × 10 px	0.035	−50%	0.0002	−90%

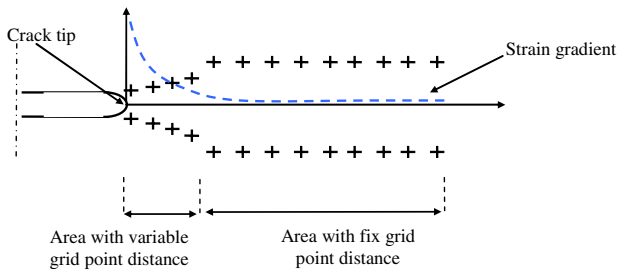

Fig. 9 Illustration of the procedure to optimize the grid-point distribution.

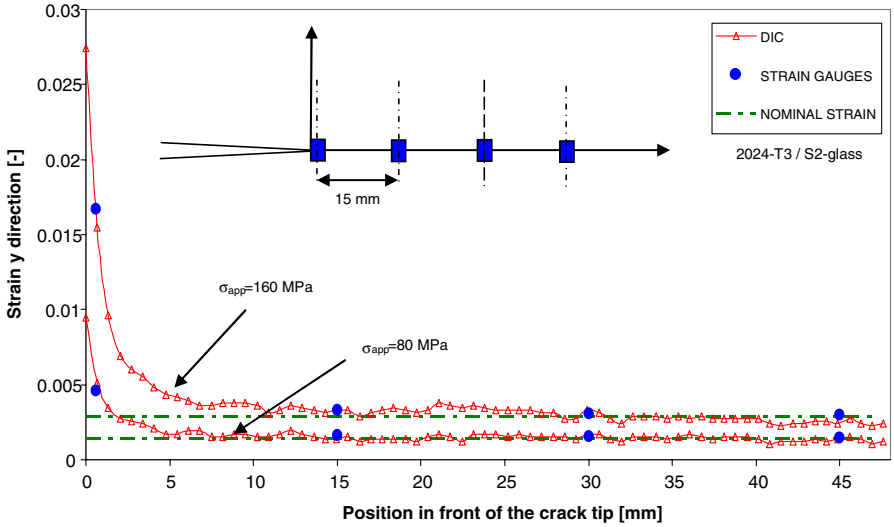

Fig. 10 Comparison of strain values obtained with DIC and with strain gauges for specimen 4.

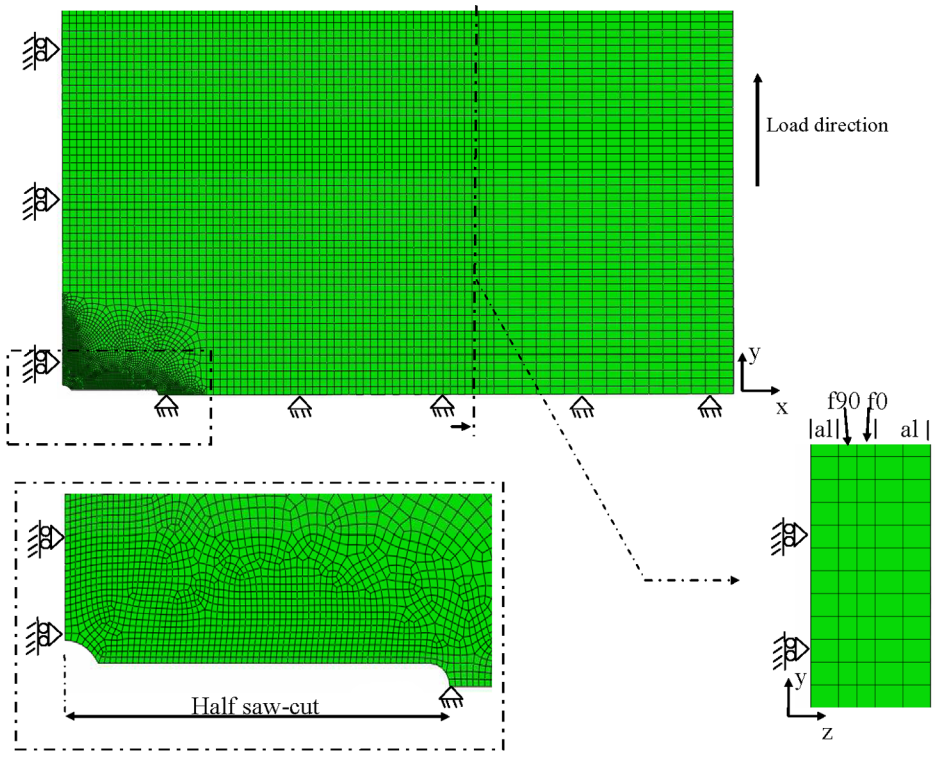

Fig. 11 Illustration of the mesh details and constrains.

Table 4 Thermal expansion coefficients referring to local coordinate system

	Ref.	α_{11}, $C^{\circ -1}$	α_{22}, $C^{\circ -1}$	α_{33}, $C^{\circ -1}$
S2 glass/FM94	[13]	$0.56 \cdot 10^{-5}$	$4.1 \cdot 10^{-5}$	$4.1 \cdot 10^{-5}$
M30SC/DT120	[a]	$-0.04 \cdot 10^{-5}$	$3.7 \cdot 10^{-5}$	$3.7 \cdot 10^{-5}$
Zylon/FM94	[14]	$-0.6 \cdot 10^{-5}$	$4.1 \cdot 10^{-5}$	$4.1 \cdot 10^{-5}$

[a]Data available online at http://www.torayca.com/index2.html [retrieved 2008].

present (e.g., ahead of the crack tip), because the strain gauges provide an averaged value of the strains underneath.

IV. Finite-Element Modeling

This section provides a brief description of the FE models created with the commercial code ABAQUS v6.8. The purpose of the FEA is to get a better understanding of the interlaminar behavior when increasing load is applied. A validation of the model has been made

Table 5 Input data for UD fiber/prepregs

UD fiber/prepreg	E_{11}, GPa	E_{22}, GPa	E_{33}, GPa	ν_{12}	ν_{13}	ν_{23}	G_{12}, GPa	G_{13}, GPa	G_{23}, GPa
S2 glass/FM94 [13]	50.6	9.4	9.4	0.33	0.33	0.0371	4	4	1.65
M30SC/DT120[a]	155	7.8	7.8	0.27	0.27	0.022	5.5	5.5	1.65
Zylon/FM94 [15]	121	2.84	2.84	0.22	0.22	0.022	1	1	1.65

[a]Data obtained from tensile tests [16].

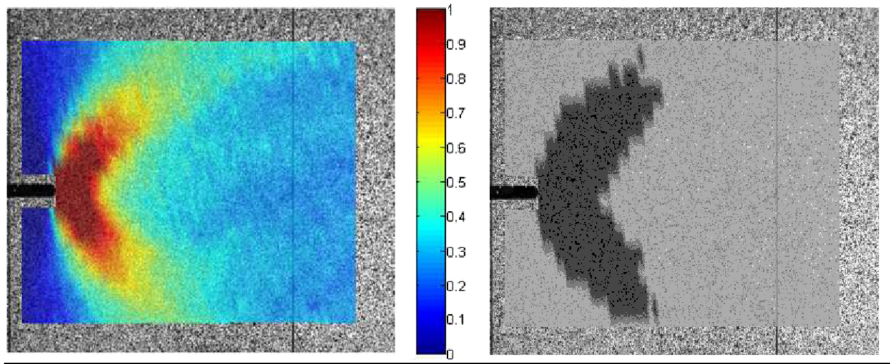

Spec.5 2024-T3

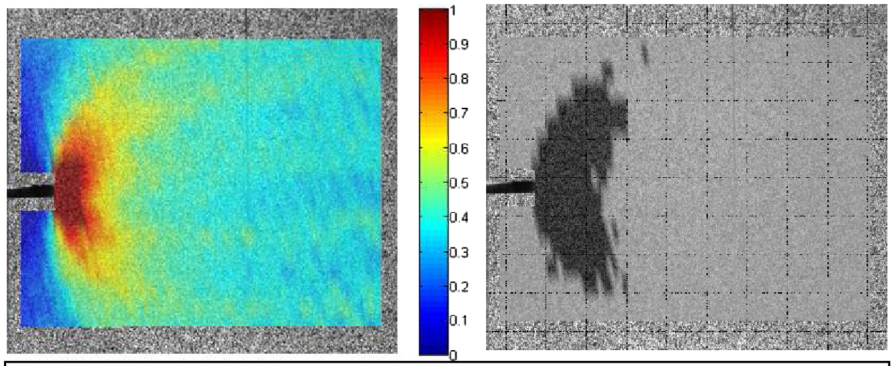

Spec.1 2024-T3/S2-glass

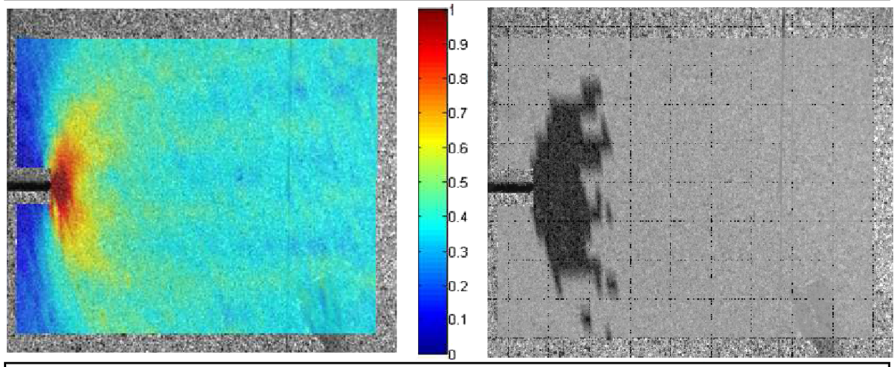

Spec.2 2024-T3/Zylon

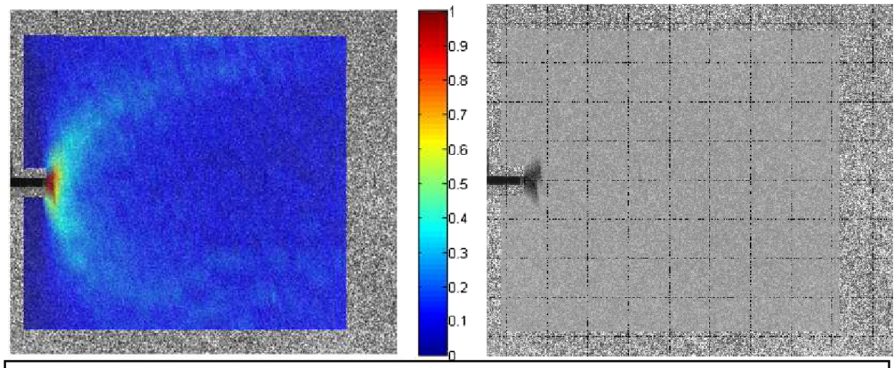

Spec.3 2024-T3/M30SC

Fig. 12 Strain fields measured experimentally, scaled from 0 to 1% (left) and related plastic zone shape (right). For all cases, the applied stress was 200 MPa.

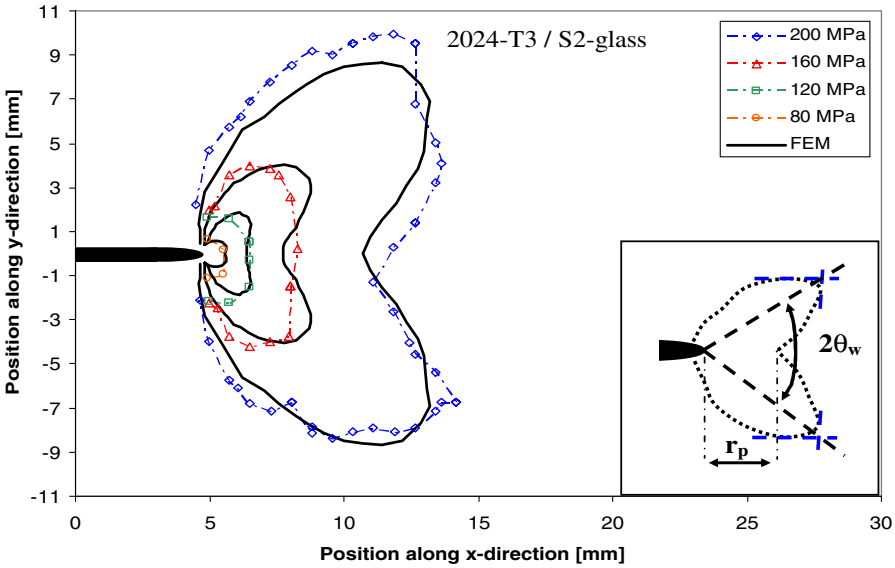

Fig. 13 Example of development of plastic zone contours at different stress levels, measured with DIC and comparison with FEA.

by comparing the calculated strain fields with those experimentally measured by means of DIC. In addition, a convergence analysis and a mesh refinement study was performed.

FE models were created for specimens 1, 2, and 3 of Table 2, using the same geometry, loads, and constraints. Because of the three symmetry planes, the geometry has been simplified by modeling only one-eighth of the full specimen and assigning a proper set of symmetry constrains along the planes, as shown in Fig. 11. The performed static analysis included six load steps, in addition to an extra initial temperature step, to take into account the residual curing stresses within the laminate due to the cooling process from 120 to 20°C. The CTE assigned for the three directions of the prepreg layers are presented in Table 4. The only stress induced in the laminate after the initial temperature step is due to the thermal contraction, without applying external load.

All mechanical properties of the 2024-T3 aluminum alloy, derived from the experimental stress/strain curve, were converted from engineering stress/strains into true stress/strains, as required by the ABAQUS preprocessor. The prepreg layers use orthotropic properties, according to the local coordinate system where the first axis is the principal. The values are reported in Table 5.

For the selection of the best meshing technique (in particular, in the vicinity of the saw cut), two approaches were followed. The first approach was to use a global model with a fine mesh and variable density of the number of elements in the area where the highest stresses were expected. The second approach used a global model

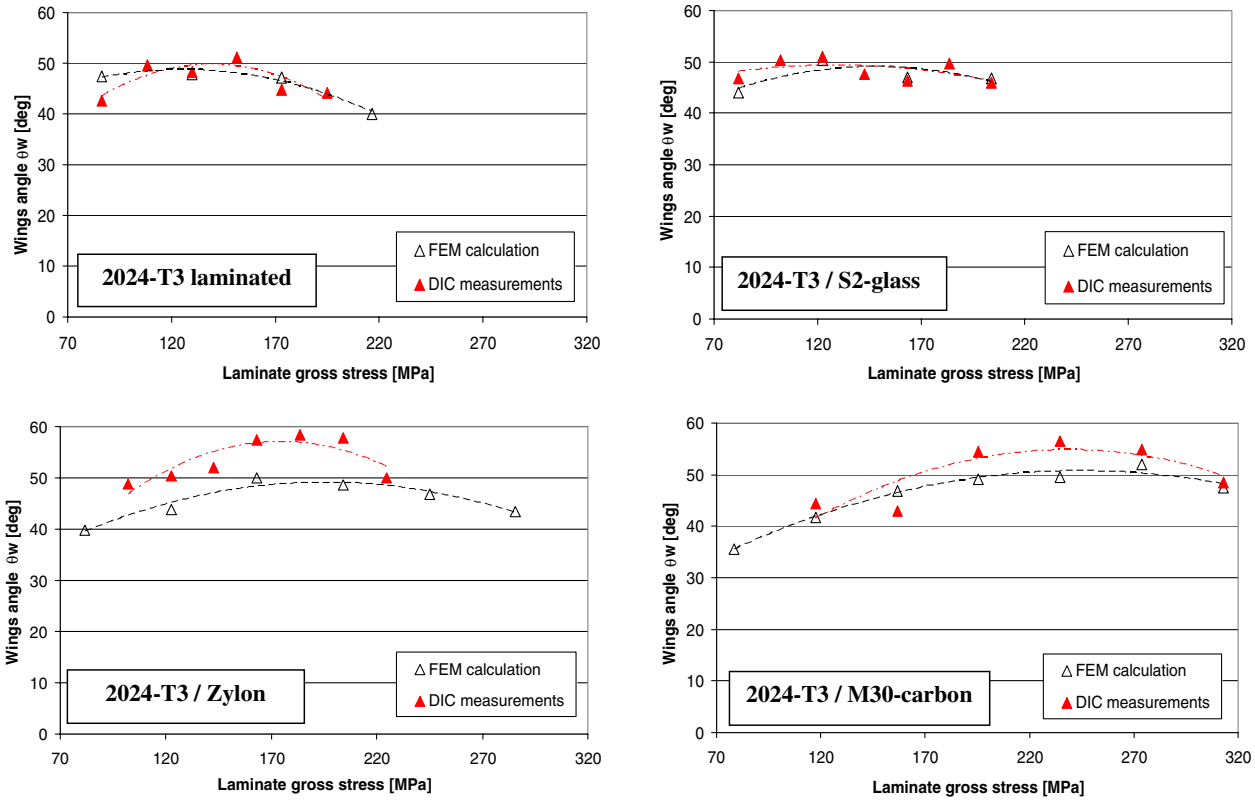

Fig. 14 Comparison between measured and predicted plastic zone wing angle for all configurations. (FEM denotes FE model.)

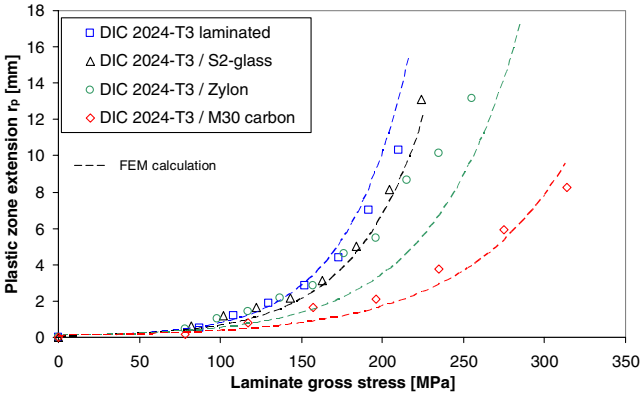

Fig. 15 Evolution of the plastic zone size for all four configurations.

with a lower number of elements and a submodel of the small part around the saw cut with a significant finer mesh. The submodel uses a solid-to-solid coupling with the global model and takes as a boundary condition the global displacements of the side nodes. This second choice implies a double run per each analysis (global model and submodel), increasing the amount of computational resources needed. A convergence study was performed on several possible meshing solutions, and the first approach was found to be the best in terms of computational time, still maintaining a good accuracy of the results. Figure 11 shows a detail of the mesh and layup of the global model. In total, 50,145 linear hexahedral elements of type C3D8R were used for the complete model, with one element through the thickness for each prepreg layer and two for the metal layers.

V. Results and Discussion

After the DIC was performed, the data was evaluated in terms of strain fields and strain gradient and compared with the FEA results.

A. Variation of the Fiber/Preimpregnated Constituent

To identify the effect of the prepreg type on the crack-tip strain field, different specimens were tested, each containing a different prepreg (specimens 1, 2, and 3 in Table 2). The left-hand side of Fig. 12 illustrates examples of strain field obtained with the DIC. The colors of the images define the strain values, which are scaled from 0 to 1%. The effect of the stiffness of the fiber/prepreg system is visible in the extension and shape of the strain field (ε_{yy}), which strongly depend on the laminate stiffness. The right-hand side of Fig. 12 shows the relative plastic zone shape, defined as the area where $\varepsilon_{yy} \geq \varepsilon_{0.2}$. The effect of the fiber/prepreg is evident when the strain fields are compared with each other and, especially, with the strain field of the 2024-T3 laminate (specimen 5).

In a 2024-T3 laminated specimen, as well as in a monolithic, the characteristic butterfly-wing shape of the strain field develops along a $\pm 50°$ angle with respect to the crack line (x direction). This characteristic behavior is related to the isotropic nature of the 2024-T3, where the plastic deformation mainly develops along the direction of maximum shear stress. When an FML is considered, the presence of an orthotropic material, like the fiber/prepreg layers, induces redistribution of the stress/strain and, consequently, variations in the strain field. In addition, the presence of fibers in the loading direction induces, to some extent, a variation of the maximum shear stress direction; therefore, the inclination of the plastic zone shape is affected as well.

Table 6 Comparison between tensile and compressive modulus [15]

FML	$E_{T\ \text{prepreg}}$, GPa	$E_{T\ \text{laminate}}$, GPa	$E_{C\ \text{laminate}}$, GPa
2024-T3/S2 glass	50	58.2	60.4
2024-T3/Zylon	120	57.1	51.9

In general, the plastic zone develops starting from a circular area, which gradually changes toward a wing shape with the load increments. This change in the shape of the plastic zone also occurs in FMLs and seems to be dependent on the stiffness of the fiber/prepreg system used. An example for the 2024-T3/S2-glass panel is provided in Fig. 13, where the experimentally measured plastic zone contours are compared with those calculated with FEA. In addition, in Fig. 13, it is illustrated how the plastic zone wings angle $2\theta_w$ and the plastic zone extension r_p are geometrically defined. Figure 14 illustrates the variation of the wing angle θ_w versus the applied stress obtained from DIC and calculated by means of FEA for all configurations.

The comparison of the experimental results with those obtained from FEA shows good agreement, except for the values measured at a low stress level. This is due to the difficulty to perform an effective measurement of plastic zones of the order of $1/2$ mm. Some of the differences between DIC and FEA are due to the absence of any failure criteria within the FE models, which do not take into account fiber failure, delamination, or metal cracking.

It can be seen that, besides the good agreement of the other configurations, the 2024-T3/Zylon configuration shows a particular behavior. For low applied stresses, the measured wing angle θ_w on the 2024-T3/Zylon configuration is similar to the one measured on the 2024-T3/S2-glass configuration. This means that, apparently, despite the different fiber stiffness, the orthotropy introduced by the fiber is similar in both cases. When high loads are applied, the measured angle in the 2024-T3/Zylon configuration increases, while in the 2024-T3/S2-glass configuration, it decreases. This means that, apparently, the laminate with Zylon fibers changes stiffness during the loading sequence, according to the nominal higher stiffness of Zylon fibers (see Table 1).

Similar behavior is visible in Fig. 15, where the plastic zone extension r_p is plotted against the laminate remote stress. Also, in this case, there is a good agreement between DIC measurements and FEM results, except for the 2024-T3/Zylon laminate. After some load increments, the trend of the laminate with Zylon fibers deviates from the trend of the other laminates (S2-glass and 2024-T3 laminates), thus behaving as a stiffer laminate. This behavior is not reproduced within the FEA.

The differences observed in the test data concerning the 2024-T3/Zylon laminate can be explained by a change of tensile behavior of Zylon fibers due to the residual stresses after the curing cycle. Once cured, the fiber layers within the laminate undergo to a compression state (due to the difference in CTE). As reported in [15], despite the relative high Young's modulus (120 GPa), the compression modulus of Zylon fibers is about half of the tensile modulus. This induces the laminate to react initially with a lower stiffness (first part of the loading sequence). When the applied load is high enough, the actual stress in the fiber layers changes from compression to tension, thus increasing the stiffness of the laminate. As shown in Table 6, the Zylon laminate shows lower tensile modulus, as well as lower compression modulus, when compared with glare.

B. Strain Gradients in Front of the Crack Tip

Figures 16a–16c compare the strain gradients in front of the crack tip for three different stress levels considering three FMLs with three different fibers types.

At low applied load, the differences between the three FMLs are small, and the Zylon configuration seems to show lower stiffness with respect to the S2-glass one. This behavior is in agreement with what is shown in Table 6. On the other hand, at higher loads, the trend of each curve changes according to the nominal stiffness of the fiber/prepreg system. The effect of the layup on the strain field ahead of the crack tip is illustrated in Fig. 16d for glare 2 and glare 3 configurations. The glare 2 laminate contains unidirectional fiber layers instead of cross ply, which is typical for glare 3. This introduces more orthotropy in the laminate, and the stiffness of the laminate increases. Consequently, a variation on the plastic zone size and shape is observed when glare 2 and glare 3 layups are compared.

The strain gradients calculated with FEA agree with the DIC measurements as long as fiber failure does not occur. An example of

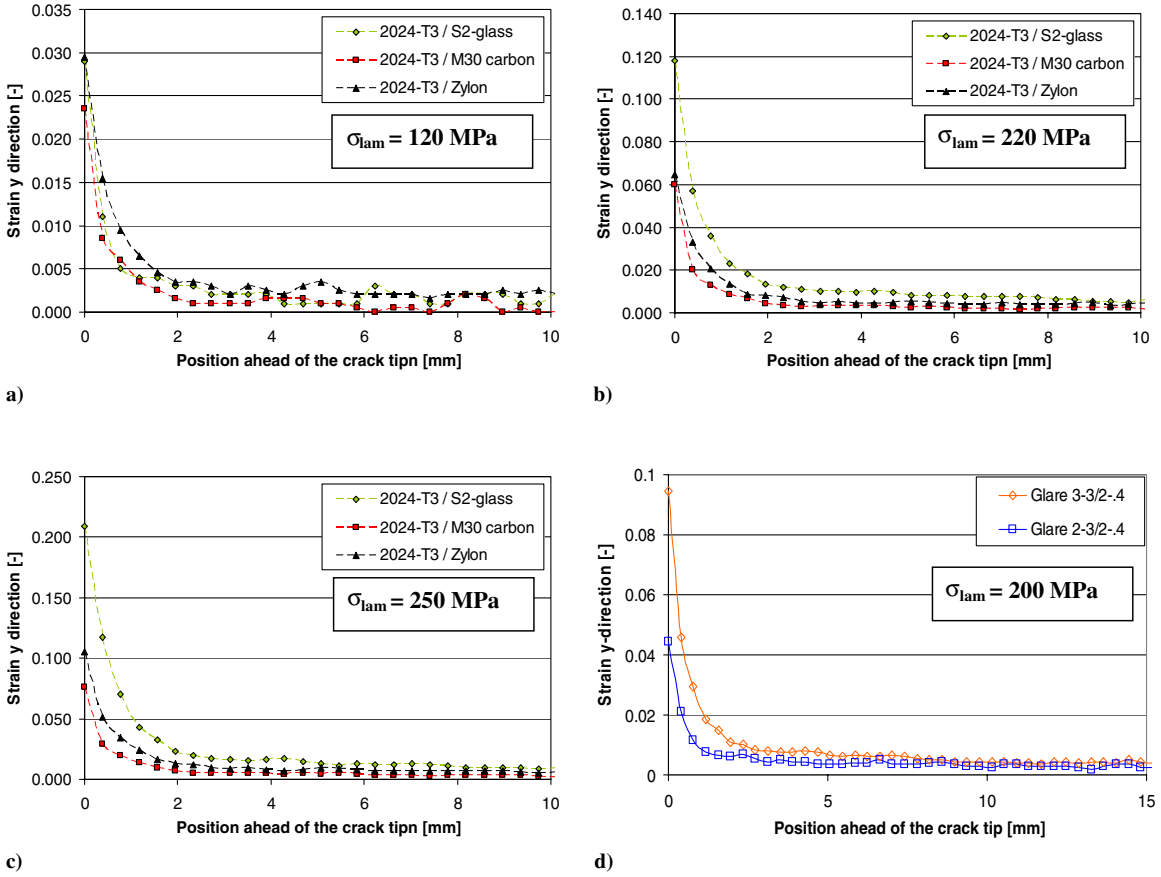

Fig. 16 Comparison of strain gradients in front of the crack tip for different applied stress and for different FML configurations.

mismatching between FEM and DIC is provided in Fig. 17 for the 2024-T3/S2-glass laminate. In an actual test, fiber failure and delamination occurs ahead of the crack tip because of the high stress/strain level, which develops when high static loads are applied. Since the FE model does not take into account any failure mechanisms, except the stiffness degradation due to metal plasticization, the calculated strain values are lower near the crack tip (see Fig. 17). Because of fiber failure (for S2 glass, it occurs at 4.5% strain), more stress/strain is transferred to the still intact metal layers.

This results in a higher strain of the metal layer, inducing differences between FEM and DIC results. Fiber failure can only be delayed in the case of local delamination at the metal/fiber interface caused by shear stresses generated inside the bond line. When the high strength of the bond line is ensured by a proper selection of the pretreatment of the metal surface (anodize plus priming [3,5]) and by the use of a high-toughness resin, the critical shear stress is higher enough that fiber failure occurs before the onset of static delamination.

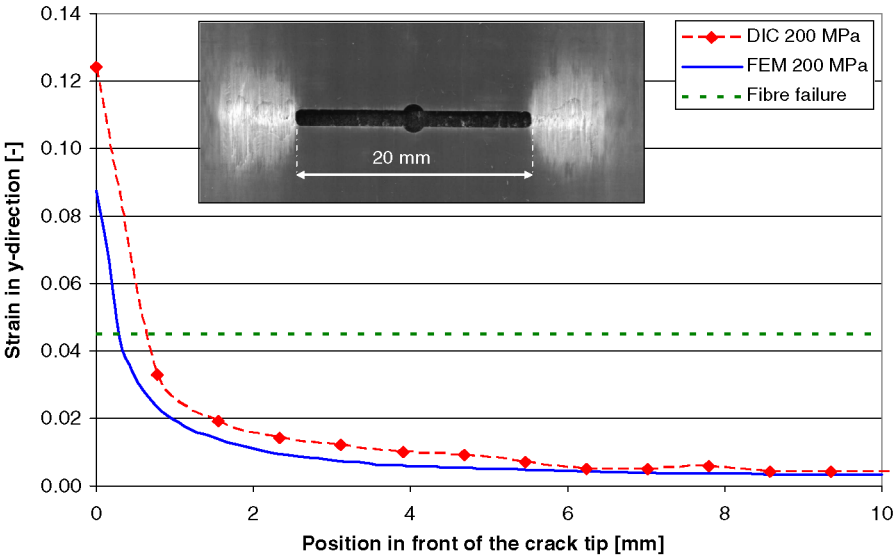

Fig. 17 Illustration of the difference between FEM and DIC due to fiber failure (2024-T3/S2 glass). Details of fiber failure and dynamic delamination in front of the crack tip after chemical etching.

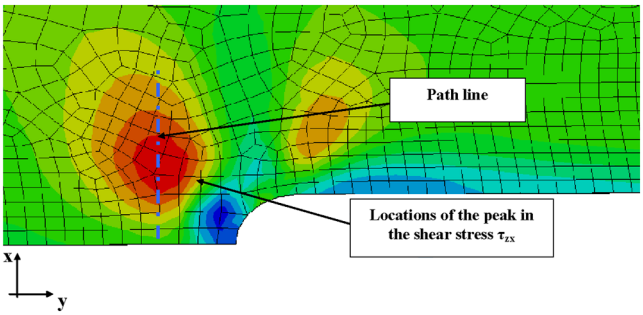

Fig. 18 Illustration of the location of the shear stress peak on the metal/fiber 0° interface. 2024-T3/S2 glass, applied load 170 MPa.

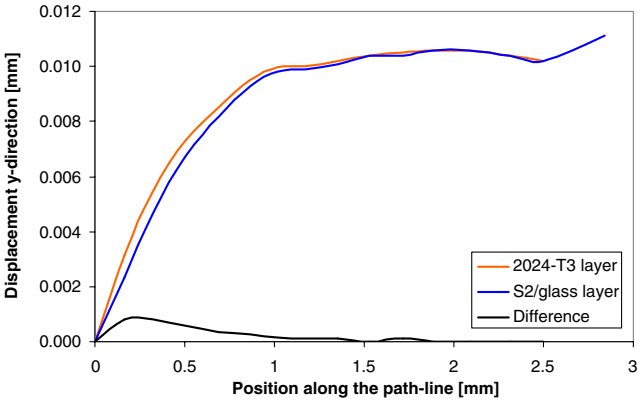

Fig. 19 Comparison of the vertical displacement between metal and fiber layers (2024-T3/S2 glass) for an applied stress of 200 MPa.

C. Shear Stress at the Metal/Fiber Interface

The FEA provided a qualitative insight into the shear mechanisms at the metal/fiber interfaces. Figure 18 shows the area of the metal/fiber 0° interface, where the shear stress peak τ_{zx} develops. To quantify the variation of the shear stress along the longitudinal direction, values of the shear stress and vertical displacement have been calculated along a vertical path line traced in front of the crack tip for both metal and fiber layers, selecting those nodes that are included in the high stress peak area.

This mechanism is induced by the load transfer due to the metal plasticization. The higher the stiffness of the fibers,the larger the amount of load transferred through the interface by shear stress. Figure 19 illustrates an example of the vertical displacements calculated along the path line for both metal and fiber/prepreg 0° layers in the 2024-T3/S2-glass laminate. The difference in displacement between the two layers is responsible for the shear deformation in the resin reach layer of the prepreg, as qualitatively illustrated in Fig. 18. This shear mechanism is therefore influenced by the relative stiffness of the metal and fiber constituents, by the residual curing stress, and by the applied load.

VI. Conclusions

Several static-load tests have been performed on different FMLs. The stress distribution between fiber and metal layers strongly depends on the relative stiffness of the constituents.

Strain field and strain gradient measurements have been performed using DIC. The influence of the fiber stiffness and fiber orientation on the plastic zone has been observed and quantified in terms of plastic zone wing angle and plastic zone size.

Despite the relatively high Young's modulus of Zylon fibers, the stiffness of the 2024-T3/Zylon laminate is comparable to the one of the 2024-T3/S2-glass laminate. This has also been observed in the plastic zone development versus the applied stress. The reason has been found in the fact that the compressive modulus of Zylon fibers is about half of the tensile modulus.

The elastic-plastic FE model has been developed and validated by comparing the predictions with the experimental results. Implementation of failure criteria, such as fiber failure, into the FE model could improve the accuracy of the prediction, especially for high applied loads.

The FEA provided further qualitative information about the interlaminar behavior. The shear stress developed at the metal/fiber interface has been related to the load transferred from the yielded metal to the elastic fibers. This is also related with the different vertical displacement between fiber and metal layers in the yielded area in the vicinity of the crack tip.

DIC is demonstrated to be a powerful strains measurement technique, providing detailed quantitative measurements of the strain field and plastic zone. Optimization of the digital grid points resulted were of extreme importance in performing an effective measurement.

The understanding of the crack-tip mechanisms is fundamental in order to assess the global behavior of a generic FML under static loading. This study provided a solid base for development of an analytical prediction model for residual strength in FMLs.

Acknowledgments

This research was carried out under project number MC1.06268, in the framework of the Research Program of the Materials Innovation Institute, the former Netherlands Institute for Metals Research. The authors acknowledge the support provided by the technical staff of the Aerospace Structure and Materials Laboratory of the Delft University of Technology.

References

[1] Anonymous, "Part 25: Damage-Tolerance And Fatigue Evaluation Of Structure," Federal Aviation Administration, Sec. 25.571, 1965.

[2] Vermeeren, C. A. J. R., "The Residual Strength of Fibre Metal Laminates," Ph.D. Thesis, Delft Univ. of Technology, Delft, The Netherlands, 1995.

[3] de Vries, T., "Blunt and Sharp Notch Behaviour of Glare Laminates," Ph.D. Thesis, Delft Univ. of Technology, Delft, The Netherlands, 2001.

[4] de Vries, T. J., and Vlot, A., "The Influence of the Constituent Properties on the Residual Strength of Glare," *Applied Composite Materials*, Vol. 8, No. 4, 2001, pp. 263–277. doi:10.1023/A:1011256202539

[5] Vlot, A., and Gunnink, J. W., *Fibre Metal Laminates an Introduction*, Kluwer Academic, Norwell, MA, 2001.

[6] Lemmen, H. J. K., Alderliesten, R. C., Benedictus, R., Hofstede, J. C. J., and Rodi, R., "The Power of Digital Image Correlation for Detailed Elastic-Plastic Strain Measurements," *Engineering Mechanics, Structures, Engineering Geology (EMESEG '08)*, Crete Island, Greece, WSEAS Press, Stevens Point, WI, 2008, pp. 73–89.

[7] Alderliesten, R. C., and Benedictus, R., "Fiber/Metal Composite Technology for Future Primary Aircraft Structures," *Journal of Aircraft*, Vol. 45, No. 4, 2008, pp. 1182–1189. doi:10.2514/1.33946

[8] Alderliesten, R. C., "Analytical Prediction Model for Fatigue Crack Propagation and Delamination Growth in Glare," *International Journal of Fatigue*, Vol. 29, No. 4, 2007, pp. 628–646. doi:10.1016/j.ijfatigue.2006.07.006

[9] "Standard Test Methods for Tension Testing of Metallic Material," , American Society for Testing and Materials, Rept. ASTM-E8M04, West Conshohocken, PA, 2004.

[10] Homan, J. J., "Fatigue Initiation in Fibre Metal Laminates," *International Journal of Fatigue*, Vol. 28, No. 4, 2006, pp. 366–374. doi:10.1016/j.ijfatigue.2005.07.030

[11] Guanchang, J., Zhen, W., Nikeng, B., and Xuefeng, Y., "Digital Speckle Correlation Method with Compensation Technique for Strain Field Measurements," *Optics and Lasers in Engineering*, Vol. 39, No. 4, 2003, pp. 457–464. doi:10.1016/S0143-8166(02)00028-3

[12] Wang, M., Cen, Y., Hu, X., Yu, X., Xie, N., Wu, Y., Xu, P., and Xu, D., "A Weighting Window Applied to the Digital Image Correlation Method," *Optics and Laser Technology*, Vol. 41, No. 2, 2009, pp. 154–158. doi:10.1016/j.optlastec.2008.05.014

[13] Alderliesten, R. C., "Fatigue Crack Propagation and Delamination Growth in Glare," Ph.D. Thesis, Delft Univ. of Technology, Delft, The Netherlands, 2005.

[14] Huang, Y. K., Frings, P. H., and Hennes, E., "Mechanical Properties of Zylon/Epoxy Composite," *Composites, Part B*, Vol. 33, No. 2, 2002, pp. 109–115. doi:10.1016/S1359-8368(01)00064-6

[15] Alderliesten, R. C., "Development of Innovative and Advanced Laminates for Future Aircraft Structures (DIALFAST)," Delft Univ. of Technology Rept. 502846, Delft, The Netherlands, 2006.

[16] "Standard Test Methods for Tensile Properties of Polymer Matrix Composite Materials," American Society for Testing and Materials Rept. ASTM-D3039, West Conshohocken, PA, 2004.